Remote Sens. **2015**, *7*, 1-x manuscripts; doi:10.3390/rs70x000x

OPEN ACCESS

remote sensing

ISSN 2072-4292

www.mdpi.com/journal/remotesensing

Article

An Empirical Study of ATCOR vs. FLAASH Atmospheric Correction for Hyperspectral Classification of Tree Species Using SVM

Morteza Shahriari Nia[1,*], Daisy Zhe Wang[1], Paul Gader[1], Stephanie Ann Bohlman[3], and Milenko Petrovic[2]

[1] Department of Computer and Information Science and Engineering, University of Florida, 432 Newell Dr., Gainesville, Florida 32611; E-Mails: msnia@cise.ufl.edu; daisyw@cise.ufl.edu; pgader@cise.ufl.edu;

[2] Institute for Human and Machine Cognition, 15 SE Osceola Ave, Ocala, Florida 34471; E-Mail: mpetrovic@ihmc.us;

[3] School of Forest Resources and Conservation, University of Florida, 349 Newins Ziegler Hall, Gainesville, Florida 32611; E-Mail: sbohlman@ufl.edu;

* Author to whom correspondence should be addressed; E-Mail: msnia@cise.ufl.edu.

Received: / Accepted: / Published:

Abstract: Identifying savannah species at the ecological scale is a key step in measuring biomass, carbon reserves, and drought and for predicting the spread of invasive species. In this paper we perform classification and geo-mapping of tree species from hyperspectral imagery collected using AVIRIS airborne sensors at pixel level. A thorough comparison of the effects of ATCOR and FLAASH atmospheric corrections on prediction accuracy is given, and Gaussian Filters have been exploited to eliminate sensor measurements and calibration errors. To the best of our knowledge we are the first in employing Gaussian Filters for hyperspectral species classification. The area of study is Ordway-Swisher Biological Station in north-central Florida. Due to the structure of the collected field data, we realized that applying NDVI and NIR filters do not play constructive roles in classification. Species classification was performed using a variety of Support Vector Machine kernels where Radial Basis outperformed others. Our classification produces accurate predictions of about 75%.

Keywords: Species classification; Atmospheric Corrections; FLAASH; ATCOR; Ordway-Swisher Biological Station; National Ecological Observatory Network;

1. Introduction

Mapping tree species by remote sensing techniques is an essential step in understanding the roles of planetary species at the ecological scale. This will enable study of land covers, climate change, invasive species, plant competitions, field fire potentials and spreading routes, and soil characteristics among others [1,2]. This kind of research has been possible only via the technological advancements in *remote sensing* facilities such as hyperspectral imagery or Light Detection and Ranging (LiDAR).

Various studies have dealt with identifying tree species both at pixel level and crown level. As technology becomes available and economically feasible, studies tend to cover larger areas and try to focus on more fine-grained details. Here we provide an overview beginning from high-level approaches to more fine-grained aspects of remote sensing of plant species using hyperspectral technologies. Carnegie Airborne Observatory[1] (CAO) is a major pioneer in employing airborne technology for remote sensing at the ecology scale, including large areas in Amazonians, Kruger National Park in South Africa, and Madagascar among others. Colgan et al. [1] used a two stage Support Vector Machine (SVM) at pixel level and at crown level for tree species classification, in which LiDAR measurements were used for crown segmentation. Féret and Asner [3] studied the accuracy of various parametric/non-parametric supervised classification techniques and observed that there is a clear advantage in using Regularized Discriminant Analysis, Linear Discriminant Analysis, and SVM. There have been other tree species classification efforts such as [3-9] that share the same approach with minor variations.

Cho et al. [3] looker deeper and compared the classification performance of different hyperspectral band ranges of CAO, WorldView2 and QuickBird. By convolving the 72 bands of CAO to eight and four multispectral channels available in the WorldView-2 and QuickBird satellite sensors, respectively, they observed that WorldView-2 produced more accurate classification results than QuickBird with CAO placing third. Clark et al. looked more into signal sources and compared lab measurements to pixel and to crown level data in an attempt to identify important wavelength regions for species discrimination. They observed that optimal regions of the spectrum for species discrimination varied with scale. However, near-infrared bands were consistently important regions across all scales. Bands in the visible region and shortwave infrared were more important at pixel and crown scales [10]. In another publication, Clark et al. evaluated the applicability of different parameters (indexes, derivatives, signal intensities) for classification [11].

Going deeper into signal details, there are reports identifying more context-specific features. Baldeck and Asner [12] tried to measure the similar beta diversity of different regions. They used distance measures such as Euclidean distance and K-means clustering in unsupervised models. Use of these clustering techniques provides a quick understanding of beta diversities; thereby avoiding costly and time-consuming field data collections. However, this line of research needs more work, as about 50% of pixels are classified as *other*. Therefore, any conclusion at this scale of uncertainty is not necessarily helpful, and the same holds in Baldeck et al.'s later work in [13]. Using the same line of

[1] http://cao.stanford.edu/

research, it is observed that different bands in a hyperspectral image have different signal-to-noise ratios. Principal Components (PC) transform will not always result in components with a steadily increasing noise level, and this makes setting a cut-off point difficult in dimensionality reduction. Minimum Noise Fraction, which is a modified PC transform, produces a set of principal component images ordered in terms of decreasing signal quality [14].

Even lower in signal level, we face the impact of the atmosphere, which is variable in space and time, and usually requires correction for quantitative remote sensing applications [15-18]. Several researchers have investigated the effects of different atmospheric correction methods for Landsat [19,20], QuickBird [21], and many other types of imaging spectrometer data [22,23]. Unfortunately none of them addresses the impact of atmospheric correction for plant species classification. The main goal of such papers, was usually bound to low level signal manipulation and estimation, as well as, at most, comparison to simple ground data such as asphalt or gravel. The final goal of atmospheric correction, which in our context is species classification, is not a well-studied subject. Some approaches to atmospheric correction include scene-derived adjustments, in which in-scene statistics are used, such as the Darkest Pixel method [21,24], or purely empirical methods where ground-recorded spectral data are required, e.g., the Empirical Line [25,26]. Some involve radiative transfer algorithms such as the 6S code [27] and MODTRAN [28], while others use in situ spectral data (model based) such as ATCOR (ATmospheric CORection) [29-32] and FLAASH (Fast Line-of-sight Atmospheric Analysis of Spectral Hypercubes) [33,34]. If ground data are not available, radiative transfer models provide a cost- and time-effective solution, as was the case in this study, and we focused on ATCOR and FLAASH. Our results align with the performance by state-of-the-art comparison of the two as in [35], where they focused on basic endmember classification (asphalt, gravel, rocky areas, reddish soil, agricultural areas, grass/dry grass, mequis, and phrygana), but we also looked into the actual problem of tree species classification.

For this study data were provided by National Ecological Observatory Network (NEON) for Ordway-Swisher Biological Station in north-central Florida, USA. Local ecological-site observations fall short on providing ecological-scale analysis of the environment. To solve this problem, NEON begins a 30-year ecology-monitoring project starting in 2016, with the goals of discovering, understanding and forecasting parameters that impact climate change, land use change, invasive species, etc at the continental-scale. Measurements and samples shall be collected using highly standardized methods and instrumentation, so that data can be used intra-site. NEON will monitor sites within 20 eco-climatic domains across the contiguous United States, Alaska, Hawaii, and Puerto Rico, coordinated with high resolution, regional airborne remote sensing observations [36]. The network will also include 40 re-locatable terrestrial sites (mobile every five to seven years) as well as 36 aquatic sites[1]. The remote-sensing Airborne Observation Platform (AOP) has instrumentation capable of meter/sub-meter resolution for hyperspectral and LiDAR measurements. This paper is a pilot study on the pre-mission airborne hyperspectral data collection. No operation at the scale and time span predicted to be fulfilled for NEON (neither geographical nor time span) has ever been carried out before [37].

[1] http://www.neoninc.org/science/domains#sthash.aW1THj1N.dpuf

Figure 1. Location of Ordway-Swisher Biological Station

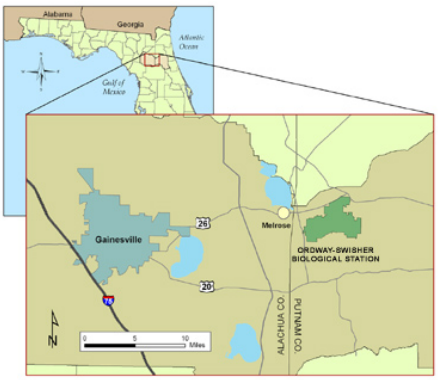

The contributions of this paper are as follows: We performed plant species classification using SVM and studied the impact of different atmospheric correction techniques (ATCOR and FLAASH) for classification accuracy. We also proposed use of Gaussian filters for de-noising reflectance values. Contrary to the general suggestion that removal of shady and non-green (low NDVI, low NIR) pixels helps classification accuracy, our results show that in certain situations it is advisable to preserve such pixels to enhance the aggregate performance of SVM. This can be helpful in finding maximum margin support vectors, thus avoiding high bias in the data (as opposed to high variance). The paper is organized as follows: Section 1 has provided an introduction to the big picture of state-of-the-art remote sensing techniques for species classification and the role of our study. In Section 2, we discuss airborne data and field data collection details. Section 3 describes atmospheric correction details, Gaussian Filtering, low NDVI and low NIR pixel impacts, and also classification function details using SVM. In Section 4, we present our results and discuss the impacts of our contributions, followed by concluding remarks in Section 5.

2. Data Collection

The NEON Southeast Domain 3 contains the southern portions of the Gulf Coast states, half of South Carolina, and all of Florida, except for the southern tip. The candidate core site for Domain 3 is located at the Ordway-Swisher Biological Station (OSBS) which is a 37 km^2 area in Putnam County in north-central Florida and is managed jointly by the University of Florida and the Nature Conservancy (Figure 1). OSBS features diverse natural forests, nearby small pine plantations, a range of wildlife species that reflects the area's ecological communities along with a 75-year history of low human impact. Florida Natural Areas Inventory defines nine major plant communities within the region which are: sandhill, xeric hammock, upland mixed forest, baygalls, basin swamp, basin marsh, marsh lake, clastic upland lake and sandhill upland lakes. The sandhill community is managed using prescribed burning on a scheduled 3-year rotation. The ground sampling part of this campaign focused on a sandhill ecosystem dominated by Long-Leaf Pine (*Pinus Palustris*) and Turkey Oak (*Quercus Laevis*) [37,38].

Since the instrumentation slated for deployment on the eventual AOP remote-sensing payloads were not yet available, airborne spectroscopic and LiDAR measurements were performed using existing

Figure 2. JPL AVIRIS flights over OSBS [37]

(**a**) Flights ground tracks.

(**b**) Hyperspectral true-color mosaic, morning 09/04/2010.

(**c**) Hyperspectral true-color mosaic, mid-day 09/10/2010.

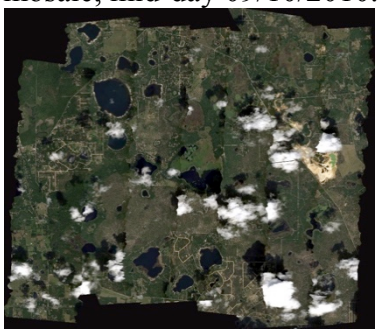

systems that exhibit similar performance characteristics as the instrumentation under development [38]. It is important to note that the actual system for NEON will have better conformance of hyperspectral/LiDAR integrations with better spatial resolution. However, here we focus only on hyperspectral data.

AVIRIS (Airborne Visible/Infrared Imaging Spectrometer) operated by the Jet Propulsion Laboratory (JPL) deployed on a Twin Otter DeHavilland DHC-6-300 aircraft in partnership with the National Aeronautics and Space Administration Terrestrial Ecology Program was used to collect data. JPL has flown on two separate days over OSBS: morning of September 4, 2010 and mid-day of September 10, 2010. Both of the flights were conducted at approximately 4000m AGL at approximately 90 knots with zenith angle of 180.0 and azimuth angle of 0.0 with altitude of 13kft (SOG ~ 65-91kts).[1] The atmospheric condition was mostly clear with some haze on September 4th and some puffy clouds on September 10th. Details of these flights can be seen in Figure 2. Dependent on flight line, pixel sizes ranged from 3.3m to 3.6m. Hyperspectral data were atmospherically corrected using FLAASH and ATCOR algorithms. Altogether, 8 flight lines and 224 bands were recorded with wavelengths from 365.93 nm to 2496.24 nm.

Atmospheric characterization relied on measurements of a CIMEL sun photometer in coordination with the NASA Aerosol Robotic Network[2]. Measurements were collected on September 4, 2010 and the derived atmospheric information was used to improve the atmospheric correction of the AVIRIS spectrometer data. Detailed measurements such as aerosol optical thickness, water vapor, etc are available online[3]. NEON personnel performed the ortho-rectification and atmospheric correction of the reflectance/radiance values.

2.1. Field Data

[1] NASA JPL AVIRIS flight details:
http://aviris.jpl.nasa.gov/cgi/flights_10.cgi?step=view_flightlog&flight_id=f100904t01
http://aviris.jpl.nasa.gov/cgi/flights_10.cgi?step=view_flightlog&flight_id=f100910t01

[2] NASA AERONET: http://aeronet.gsfc.nasa.gov/cgi-bin/bamgomas_interactive

[3] OSBS Aero Measurements: http://aeronet.gsfc.nasa.gov/cgi-bin/type_one_station_opera_v2_new?site=Ordway-Swisher

Geo-identification of tree species as field data was performed on February 28th, 2014. A laptop preloaded with ArcMap and ENVI software was used in conjunction with a professional grade GPS. ArcMap reads GPS coordinates and maps identified canopy polygons in ENVI, which is pre-loaded with relevant flight data. In this way, we marked several geo-polygons having similar plant species in ENVI. Later, we overlaid the identified polygons with proper JPL AVIRIS flight data with the least degree of cloudiness. This approach works fairly well when not in a dense forest, such as a tropical forest, where the GPS signal under the tree canopy has high deviations due to NLOS (no-line of sight). One should note that even with these considerations, commercial GPS have sub-meter accuracy and when combined with error accumulated in ortho-rectification of flight images, it was still necessary to mark several distinct features, such as roads, large trees or other land marks, to be able to re-verify marked points on the map and avoid shifts in coordinates. Altogether species were identified for 1269 pixels. Details of the identified Regions of Interest (ROIs) are presented in Table 1.. The closer ROI Ids were collected from closer vicinity (geographically/temporally), and the more distant ROI Ids indicate that the canopies were more separated.

Figure 3. Field Data Distribution of ROIs.

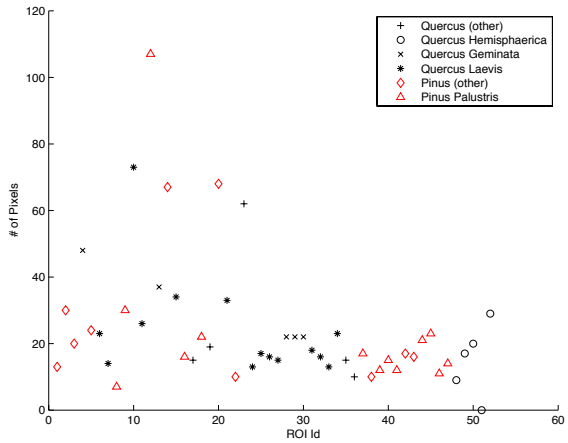

Table 1. Field Data Specifications

	Broadleaf								**Conifer**			
Specie	Oak (other)		Laurel Oak		Live Oak		Turkey Oak		Pine (other)		Longleaf Pine	
	ROI Id	Pixels	ROI Id	Pixels	ROI Id	Pixels	ROI Id	Pixels	ROI Id	Pixels	ROI Id	Pixels
	23	62	52	29	4	48	10	73	20	68	12	107
	19	19	50	20	13	37	15	34	14	67	19	30
	17	15	49	49	28	22	21	33	2	30	45	23
	35	15	48	9	29	22	11	26	5	24	18	22
	36	10	53	6	30	22	6	23	3	20	44	21
							34	23	42	17	37	17
							31	18	43	16	16	16
							25	17	1	13	40	15
							26	16	22	10	47	14
							32	16	38	10	39	12
							27	15			41	12
							7	14			46	11
							24	13			8	7
							33	13				
Total	5	121	5	81	5	151	14	334	10	275	13	307
Partial Total	29 ROIs – 687 Pixels								23 ROIs – 582 Pixels			
Grand Total	52 ROIs – 1269 Pixels											

Some species are abundant (e.g. 334 for Turkey Oak) where others are less so (e.g. 81 for Laurel Oak). This bias in population size inadvertently affects classification accuracy. Figure 3 depicts the abundance of each canopy respectively. The Oak (other) species represent generic oak specie (*specie details unknown*). Live Oak is specifically Sand Live Oak (*Quercus Geminata*), Laurel Oak represents *Quercus Hemisphaerica*, Turkey Oak is *Quercus Laevis*, Longleaf Pine is *Pinus Palustris*, and Pine (other) represents a mixture of different varieties of pines: Longleaf Pine (*Pinus Palustris*), Loblolly Pine(*Pinus Taeda*) or Slash Pine (*Pinus Elliotti*).

3. Species Classification

Due to the large size of each pixel (3+ by 3+ square meters) pure pine or oak signals were not obtained, and there were many linear/nonlinear mixtures of endmembers in each pixel (e.g. road, shadow, branch, under-score vegetation, multiple tree species, etc.). The timing of fights (September) added to the challenge; leaves may not have been as green as earlier in the season or some trees may have already started to lose leaves, potentially leading to more branch or dead leaf signals. One should note that the more leaves a tree has and the greener the leaves are, the better will be the signal in the green/visible bands, which are not absorbed by dead leaves, branches or soil. A higher absorption in the green spectral region can greatly help differentiating plant signals from surrounding endmembers. Also, the pine species have needle-like leaves, which provide minimal leaf area index compared to broadleaf species. Thus, more branch and soil signals may be present due to the structure of the leaves.

3.1. Atmospheric Correction

Ground spectral measurements regarding atmospheric correction were collected concurrently with flight operations, as described in *OSBS Aero Measurements*. Unlike many other atmospheric correction algorithms that interpolate radiation transfer properties from a pre-calculated database of modeling results, FLAASH incorporates the MODTRAN radiation transfer code. Based on any of the standard MODTRAN model atmospheres and aerosol types specified, a unique MODTRAN solution is computed for each image. FLAASH (Elexis Inc.) also includes the following features: correction for pixel mixing due to scattering of surface-reflected radiance, computation of a scene-average visibility (aerosol/haze amount), handling of stressing atmospheric conditions (e.g. presence of clouds), cirrus and opaque cloud classification mapping, and adjustable spectral polishing for artifact suppression.

FLAASH starts from a standard equation for spectral radiance at a sensor pixel, L, that applies to the solar wavelength range (thermal emission is neglected) and flat, Lambertian materials or their equivalents, as follows [33]:

$$L_e \approx \left(\frac{(A+B)\rho_e}{1-\rho_e S} + L_a\right) \quad (1)$$

where ρ_e is an *average* surface reflectance for the pixel and a surrounding region, S is the spherical albedo of the atmosphere, L_a is the radiance back scattered by the atmosphere, and A and B are

coefficients that depend on atmospheric and geometric conditions but not on the surface. Solving for surface reflectance ρ_e, we have:

$$\rho_e \approx \frac{L_e - L_a}{A + B + S(L_e - L_a)} \tag{2-a}$$

ATCOR (ATCOR 4) has the following features: capability of combination with geometric information of terrain, a lookup table of a wide range of pre-calculated radiative transfer runs for different weather conditions and sun angles employing MODTRAN, incorporation of spatially varying aerosol conditions, and statistical haze removal that masks haze and cloud regions and removes haze of land areas. It also accounts for de-shadowing of cloud/building cast shadow areas, cirrus cloud removal, BRDF correction of irradiance effects, evaluation of atmospheric parameters (aerosol type, visibility, water vapor) by comparing retrieved reflectance with library spectra, and finally, inclusion of a solar reference spectrum. ATCOR performs atmospheric correction for surface reflectance, ρ, disregarding the adjacency component, as follows [39]:

$$\rho \approx \frac{\pi(d^2(c_0 + c_1 DN) - L_{path})}{\tau E_g} \tag{2-b}$$

where τ is the atmospheric (direct or beam) transmittance for a vertical path through the atmosphere, d is the earth-sun distance in astronomical units, c_0 , c_1 and $DN$are the radiometric calibration offset, gain, and recorded brightness (digital number), respectively; and E_g is the global flux on the ground.

3.1. Signal Pre-processing

The hyperspectral images were loaded in Matlab using an in-house upgraded version of `enviread`, initially developed by Dr. Ian Howat at Ohio State University [40]. A check for the consistency of calibration and uniformity of pixel sizes indicated a range of 3.3m to 3.6m pixel sizes due to various flight and measurement conditions. As different flights have different altitudes and hence pixel resolutions, this is an essential step to take into account. Here, we define a hyperspectral image I with dimensionality (x,y,w,z), where $x \in X = [167000, 833000]$represents the range of UTM Easting values, $\mathrm{y} \in \mathrm{Y} = [0, 9400000]$ represents UTM Northing values, $\mathrm{w} \in \mathrm{W} = \{1, \cdots, 224\}$ is the index of the reflectance wavelengths, and $\mathrm{z} \in \mathrm{Z} = \{1, \cdots, 60\}$ is the UTM zone of the image. Based on our observations, the constant $\xi = 10000$ was used as a cut-off point to avoid erroneous sensor readings. There was some noise in the JPL AVIRIS measurements such as negative reflectance values; the range of hyperspectral reflectance values was $[-32762, 32724]$. Reflectance is the proportion of sun radiance signals, which should be a positive value, but in normalized form reflectance is between zero and one. The normalization process is given by:

$$I_{xywz} = \begin{cases} 0 & for\ I_{xywz} < 0 \\ 1 & for\ I_{xywz} > \xi \\ \sqrt{\frac{I_{xywz}}{\xi}} & otherwise \end{cases} \tag{3}$$

For normalization, the negative reflectance values were set to zero and values greater than 10,000 were set to 10,000. To enhance the intensity of readings the square-root of signal returns was used, due to the following facts: 1) There is no standard output of reflectance data, and even reflectance of a single crown at different pixels can be quite different. Unlike minerals that have fixed and known reflectance values, trees can give different signal returns based on generation, number of leaf layers for the crown, leaf formation and orientation, leaf area index, condition of growth (water quality, climate, soil) etc, which can make this task challenging. 2) Due to the resolution of images, signals are all mixtures of several endmembers. Due to these reasons, empirically obtained thresholds and ranges are inevitable. Regarding square root, one should note that without taking the square root, the images lack proper day-light intensity and appear dark. We excluded wavelengths corresponding to strong water vapor absorption bands in the atmosphere: 1333.2 nm to 1482.7 nm, 1791.6 nm to 1967.4 nm, and 2406.9 nm to 2496.2 nm. Due to strong absorption at those wavelengths, the instrument measures a small radiance signal.

3.1.1. Impact of Non-vegetated/Shaded Pixels

A filter of NIR < 0.33 excludes heavily shaded samples which usually have distorted reflectance signals [1]. The Normalized Difference Vegetation Index (NDVI) shows how green a pixel is and is usually used to remove material that does not belong to planetary material, such as roads, clouds and any non-vegetated area, even grass. NDVI is defined as:

$$NDVI = \frac{NIR - VIS}{NIR + VIS} \tag{4}$$

where is NIR the reflectance in the reflective near-infrared wavelengths (725-1100 nm) and VIS is the reflectance in the visible (red) wavelengths (580-680 nm). The principle behind this is that VIS is in a part of the spectrum where chlorophyll causes considerable absorption of incoming radiation, and the NIR is in a spectral region where spongy mesophyll leaf structure leads to considerable reflectance [41,42]. For this purpose, the band at 665.6 nm was chosen for red and 734.1 nm for near-infrared. Filtering out pixels with NDVI < 0.4 essentially removes pixels that are not green. By properly applying an NDVI filter globally to an entire flight line, only the major tree crowns remain. However, in our scenario we observed that preserving low NDVI/NIR pixels from ground data actually helps prediction accuracy. As shown in Table 1, there are tens of pixels per ROI, and considering that each pixel is about 3m wide and that species of this study do not have wide crowns; this means that ROIs are generously marked and span across several neighboring tree crowns. This includes the empty spaces between crowns, shady pixels, understory grass, etc. The initial expectation is to remove low NDVI pixels from such large canopies to properly classify tree species. However, due to the mixing nature of hyperspectral pixels and aggregate operation of classification techniques in multi-dimensional space, removing low NDVI pixels from *tree canopies* degraded classification performance by about 10%. Therefore, it is better to preserve low NDVI pixels in this scenario, as they are mixed in with actual green pixels of trees and provide added value in the aggregate operation of SVM.

2.1.2. Gaussian Filter

Real-life sensor measurements are far from perfect, and there are many noisy readings along different bands. We take advantage of abundance of bands and exploit their local-aggregated information by applying a Gaussian filter. Taking a Gaussian window w of size $N > 0$, the coefficients of the Gaussian window are computed as:

$$w(n) = e^{-\frac{1}{2}(\alpha\frac{n}{N/2})^2} \quad (5)$$

where $-\frac{N-1}{2} \leq n \leq \frac{N-1}{2}$, and α is inversely proportional to the standard deviation (σ) of a Gaussian random variable ($\sigma = \frac{N}{2\alpha}$). After Gaussian parameters are specified, convolution is performed to apply the smoothing factor. Convolving vectors $u \in R^m$ and $v \in R^n$ gives vector $w \in R^{m+n-1}$ such that:

$$w(k) = \sum_j u(j)v(k-j+1) \quad (6)$$

3.2. Support Vector Machine

It is well known in the literature that Support Vector Machine (SVM) outperforms other algorithms on species classification [1,13,43]. Our focus is on the impact of atmospheric correction (specifically FLAASH vs ATCOR) at pixel level classification using non-linear multi-class SVM. We parameterize SVM with k-fold cross validation where $k = 5$. Classifier non-linearity comes from taking the following non-linear functions as kernel for SVM:

- Polynomial function kernel.
- Radial Basis Function (RBF) kernel

Regarding multi-class classification, $\binom{c}{2}$ classifiers are created, where c is the number of classes (6 in this case). Hence, we train 15 disjoint binary classifiers at each iteration of k-fold. All the classifiers are trained, and to decide on the class of a given test pixel, majority voting among classifiers decides the class assignment. Aggregation of classes of canopy pixels is avoided to determine the class of the whole canopy. This process can be performed using well known approaches such as majority of pixels, etc., which is not relevant to the purpose of this paper. Furthermore, the assumption that the exact boundary of every single tree is known before hand does not always hold, specifically in dense vegetation; so crown-level classification is omitted from our discussion.

4. Results and Discussion

In this part we empirically evaluate the impact of optimizing classifier parameters with regard to FLAASH and ATCOR atmospheric corrections. As atmospheric correction is a low level signal processing technique, our focus in comparing the two correction methods is the impact of data pre-processing filters on the performance of the species classification. An implementation of a one-vs-one multi-class k-fold cross-validation setup of SVM using non-linear kernels (polynomial and radial basis) functions is used as the model. Majority vote among classifiers determines the specie of a pixel. Because some of the species are included in at most 5 canopies, $k > 5$ cannot be used for a correct implementation of

Figure 4. Impact of Gaussian Filter on Prediction Accuracy.

(**a**) Before removing water absorption bands. (**b**) After removing water absorption bands.

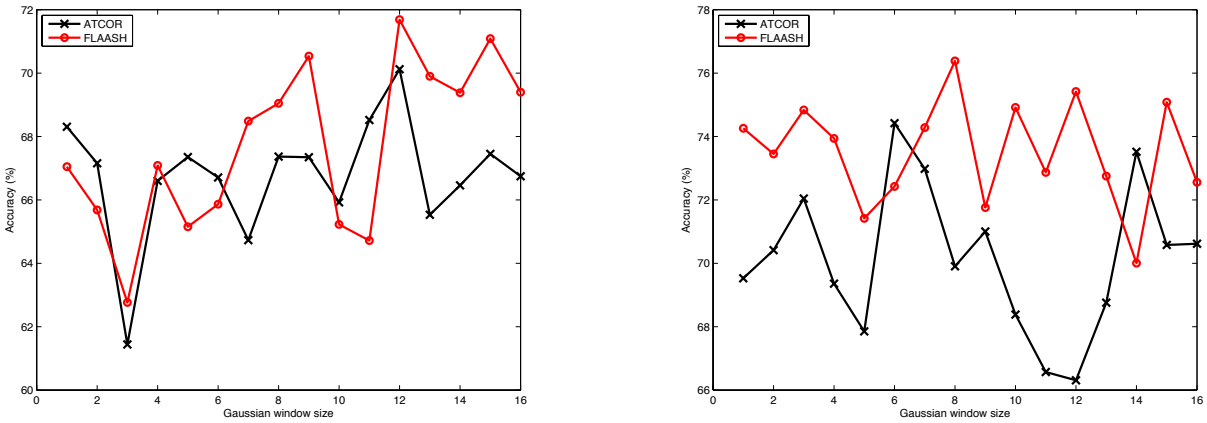

k-fold cross validation, and therefore k is set at $k = 5$. Test and train sets are canopy-aware, meaning that pixels of a single canopy are used for either training or test sets, not both. As pixels of one canopy can have many similarities, it is not advisable to use some pixels of a canopy for training and other pixels of the same canopy for test purposes. This could have the same meaning as using the same data for both training and testing, which leads to over fitting and erroneous accuracy results. A mixture of grid search and heuristic optimization determines various parameters for SVM kernels, but for brevity only 2D diagrams are presented here, as other parameters settings are beyond the scope of this project. Specifically, a cost of $C = \infty$ for is set for misclassification, meaning there is little to zero tolerance for improperly classified samples.

Figure 4 shows how removing water absorption bands helps improve prediction accuracy. Before removing these bands (Figure 4.a) prediction accuracy starts at about 66% and rises to about 71% as the Gaussian window size is increased (about 5% performance improvement). There is a positive trend across different window sizes, indicating that better accuracy can be achieved for larger window size. This stems from the fact that water absorption bands add to randomness and as the window size is increased, this randomness is dissolved to the majority of neighbors and has less and less impact. After removing water absorption bands (Figure 4.b) prediction accuracy starts at 74% and rises to about 76.5% at a window size of 8. Beyond that there is no significant change in accuracy. As window size increases there is no predictable impact of Gaussian smoothing on accuracy, because all the currently available data signals have some level of inherent entropy (reduced noise), increasing the window size beyond a certain point just takes valuable information away from the signals (increase the noise), and this can factor in accuracy in unpredictable ways. Before removing water absorption bands, FLAASH shows minor advantages over ATCOR, but after removal this difference becomes a meaningful 4% better prediction accuracy for FLAASH.

Next, the impact of removing low NDVI-NIR pixels from dataset is considered. As shown in Figure 5, there is a general degradation of performance from the previous scenario, which contained the whole dataset. In the FLASSH dataset, the accuracy is about 70%, and ATCOR yields 66% accuracy. This is due to the fact that pixel size is large (3m) and canopies are large as well (in the range of [6,107], as shown in Table 1). This generous marking of canopies includes areas with little

Figure 5. Impact of removing low NDVI and NIR pixels among field data

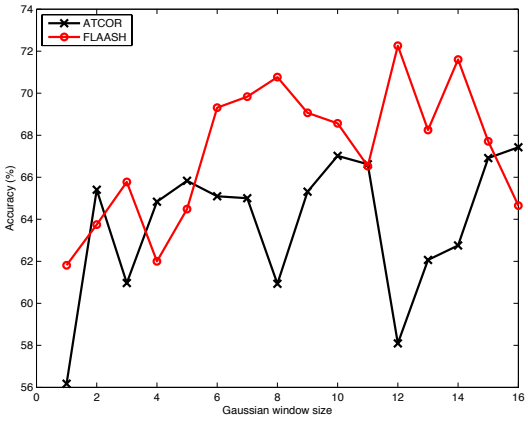

greenness (shadows, branches, gravel etc; all with low NDVI and low NIR values). But due to the mixing nature of reflectance values, even low NDVI/NIR pixels of a continuous canopy still contain signals from the underlying species, which may not be as green. Figure 5 shows that removing low NDVI/NIR pixels of a continuous canopy actually degrades the performance of the classification model with an impact of about 4%. So in similar scenarios where *field data* consists of large continuous canopies, we advise preserving low NDVI/NIR pixels. It is important to realize that this is only relevant in the context of field data, as the species are already known, and is only useful in training the classifier. In global application of NDVI/NIR filters to entire flight lines, we suggest using the method in the literature; i.e., deletion of low values to remove roads, grass, etc. Here the benefit of FLAASH over ATCOR can again be observed on average by 2%-3%.

Finally, the effect of atmospheric correction on prediction accuracy vs classification model parameters is considered. C, σ, P, MaxIter and o*ptimization method* are the knobs of SVM that are tuned in a mixture of grid and heuristic search. Here C stands for the cost or penalty of misclassification against simplicity of the decision surface; σ (or also known as γ in the literature) defines how far the influence of a single training example reaches, with low values meaning 'far' and high values meaning 'close' in RBF function; P is the polynomial degree for polynomial function as kernel; MaxIter is the maximum number of iterations the optimization function is supposed to run; and *optimization method* defines the selected optimization method. In this work, we set C=+∞, MaxIter=10,000 and use quadratic programming as *optimization method*. In the following paragraphs, we evaluate the impact of P and σ, respectively.

Figure 6.a demonstrates the impact of polynomial degree P on prediction accuracy using a polynomial kernel in SVM. FLAASH atmospherically corrected data yields 73.5% accuracy whereas ATCOR results in 69.8%. The simpler the polynomial, the better the performance; a more complicated polynomial leads to a high bias classification model which performs poorly when evaluated on test data. For FLAASH atmospheric correction ($P \geq 3$) the optimization function does not converge. On the other hand, ATCOR data performs as predicted. Accuracy drops as low as 10.8% and 11.3% with polynomial degrees of 7 and 8 (due to extreme over-fitting).

The Radial Basis kernel has better performance yields than a polynomial. As shown in Figure 6.b, the best results are achieved using FLAASH data, with a peak at 75.3%, while ATCOR comes close at 74.9%. RBF does not show good performance at σ values which are either excessively low or high,

Figure 6. Parameter tuning for classification algorithms.

(**a**) Tuning P for SVM with polynomial kernel function.

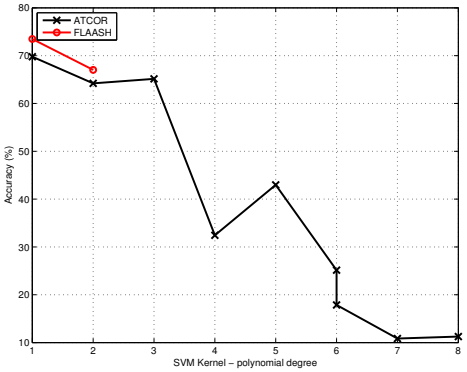

(**b**) Tuning σ in SVM with RBF kernel function.

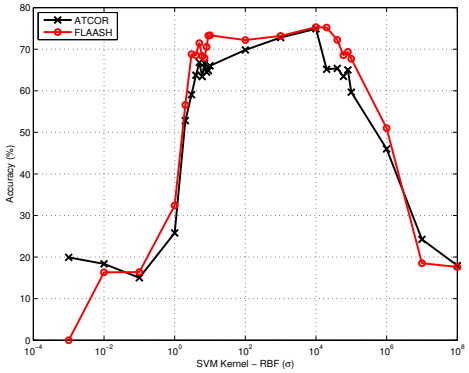

where σ is the inverse of the width of the RBF kernel (roughly defining the area of influence of a support vector); in other terms, it defines the degree of influence of a single training example. The larger σ is, the closer other examples must be to be affected. Because RBF takes data to a higher dimensionality, a small σ gives a pointed bump in the higher dimensions, and a large σ gives a softer, broader bump. Thus, neither extreme shows a good fit and a middle point of σ =10,000 provides the best results. On the negative side, FLAASH begins with an accuracy of 0% and ATCOR at 19.9%, but they quickly attain a stable region close to each other, while FLAASH demonstrates superior performance in most of the cases. There is a good range of σ values ([10, 10000]) which give a plateau in prediction accuracy, implying a more robust performance than polynomial.

Table 2 demonstrates the confusion matrix of the proposed classification model at a near peak setup (75.2%). The majority of misclassifications are between Pine (other) class and Longleaf Pine. A similar misclassification can be observed between Oak (other) and other types of Oak. This is due to the fact that this class of Oak or Pine contains a mixture of different types of Oak or Pine, respectively, which may include Longleaf Pine or Laurel Oak. Thus, such conformance may be unavoidable. The major advantage of this experiment is that there is minimal misclassification between the oak vs. pine categories. The oak category is rarely misclassified as pine, but pines have been misclassified as Turkey Oak and Laurel Oak. One should also note that there is no intra-oak misclassification of different species. Laurel Oak, Turkey Oak and Live Oak are well separable from each other, indicating a good intra broad-leaf species classification.

Table 2. Confusion Matrix for Species Classification

		Predicted Class						
		Pine (other)	Longleaf Pine	Turkey Oak	Live Oak	Oak (other)	Laurel Oak	Sum
Known Class	Pine (other)	10	10	3	0	0	0	23
	Longleaf Pine	20	36	0	0	0	4	60
	Turkey Oak	1	0	62	0	0	0	63
	Live Oak	0	0	44	4	0	0	48
	Oak (other)	0	0	0	0	1	9	10
	Laurel Oak	1	0	0	0	0	5	6
	Sum	32	46	65	44	5	18	210

In our experiments we observed better performance of FLAASH atmospherically corrected data versus ATCOR. This is in conformance with recent observations of Manakos et. al. [35] where they focused on basic endmember classification (asphalt, gravel, rocky areas, reddish soil, agricultural areas, grass/dry grass, mequis, and phrygana). However, we looked into the actual problem of tree species classification.

5. Conclusions

Identification of species using remote sensing technologies such as hyperspectral and LiDAR sensors has critical utility in studying global warming, bio-mass estimation, carbon preserves, invasive species identification, etc. In this paper, we report species classification using SVM over AVIRIS hyperspectral data available for Ordway Swisher Biological Station in north-central Florida. Our focus is on comparing FLAASH and ATCOR atmospheric corrections, while we propose using Gaussian filter for de-noising reflectance values. We also discuss how incorporating even low NDVI and low NIR pixels can be helpful in improving classification accuracy in large canopy areas. Due to the mixing nature of remote sensing hyperspectral data, using such pixels can reduce the bias in maximum margin support vectors in SVM. This observation shows a clear advantage to the use of FLAASH vs. ATCOR, by margins of about 2% to 4%. Our classification model is robust for intra-oak species classification; with minor inter-conifer/broad-leaf misclassified labels.

Acknowledgments

Authors are thankful to NEON Inc. for providing hyperspectral data. Also they are thankful to Ms. Sarah Graves, Ms. Leila Kalantari and Dr. Stephanie Bohlman for providing field data. The National Ecological Observatory Network is a project sponsored by the National Science Foundation and managed under cooperative agreement by NEON, Inc. The NEON 2010 Pathfinder data set is based on work supported by the National Science Foundation under Grant DBI-0752017.

References

1. Colgan, M.S.; Baldeck, C.A.; Féret, J.-B.; Asner, G.P. Mapping savanna tree species at ecosystem scales using support vector machine classification and brdf correction on airborne hyperspectral and lidar data. *Remote Sensing* **2012**, *4*, 3462-3480.
2. Scholes, R.; Archer, S. Tree-grass interactions in savannas. *Annual review of Ecology and Systematics* **1997**, *28*, 517-544.
3. Féret, J.-B.; Asner, G.P. Tree species discrimination in tropical forests using airborne imaging spectroscopy. *Geoscience and Remote Sensing, IEEE Transactions on* **2013**, *51*, 73-84.
4. Dalponte, M.; Ørka, H.O.; Ene, L.T.; Gobakken, T.; Næsset, E. Tree crown delineation and tree species classification in boreal forests using hyperspectral and als data. *Remote sensing of environment* **2014**, *140*, 306-317.
5. Féret, J.-B.; Asner, G.P. Semi-supervised methods to identify individual crowns of lowland tropical canopy species using imaging spectroscopy and lidar. *Remote Sensing* **2012**, *4*, 2457-2476.
6. Ghosh, A.; Fassnacht, F.E.; Joshi, P.; Koch, B. A framework for mapping tree species combining hyperspectral and lidar data: Role of selected classifiers and sensor across three

spatial scales. *International Journal of Applied Earth Observation and Geoinformation* **2014**, *26*, 49-63.
7. Immitzer, M.; Atzberger, C.; Koukal, T. Tree species classification with random forest using very high spatial resolution 8-band worldview-2 satellite data. *Remote Sensing* **2012**, *4*, 2661-2693.
8. Naidoo, L.; Cho, M.; Mathieu, R.; Asner, G. Classification of savanna tree species, in the greater kruger national park region, by integrating hyperspectral and lidar data in a random forest data mining environment. *ISPRS Journal of Photogrammetry and Remote Sensing* **2012**, *69*, 167-179.
9. Ustin, S.L.; Gitelson, A.A.; Jacquemoud, S.e., phane; Schaepman, M.; Asner, G.P.; Gamon, J.A.; Zarco-Tejada, P. Retrieval of foliar information about plant pigment systems from high resolution spectroscopy. *Remote Sensing of Environment* **2009**, *113*, S67-S77.
10. Clark, M.L.; Roberts, D.A.; Clark, D.B. Hyperspectral discrimination of tropical rain forest tree species at leaf to crown scales. *Remote sensing of environment* **2005**, *96*, 375-398.
11. Clark, M.L.; Roberts, D.A. Species-level differences in hyperspectral metrics among tropical rainforest trees as determined by a tree-based classifier. *Remote Sensing* **2012**, *4*, 1820-1855.
12. Baldeck, C.A.; Asner, G.P. Estimating vegetation beta diversity from airborne imaging spectroscopy and unsupervised clustering. *Remote Sensing* **2013**, *5*, 2057-2071.
13. Baldeck, C.; Colgan, M.; Féret, J.-B.; Levick, S.; Martin, R.; Asner, G. Landscape-scale variation in plant community composition of an african savanna from airborne species mapping. *Ecological Applications* **2014**, *24*, 84-93.
14. Green, A.A.; Berman, M.; Switzer, P.; Craig, M.D. A transformation for ordering multispectral data in terms of image quality with implications for noise removal. *Geoscience and Remote Sensing, IEEE Transactions on* **1988**, *26*, 65-74.
15. Liang, S.; Fang, H.; Chen, M. Atmospheric correction of landsat etm+ land surface imagery. I. Methods. *Geoscience and Remote Sensing, IEEE Transactions on* **2001**, *39*, 2490-2498.
16. Ouaidrari, H.; Vermote, E.F. Operational atmospheric correction of landsat tm data. *Remote Sensing of Environment* **1999**, *70*, 4-15.
17. Ju, J.; Roy, D.P.; Vermote, E.; Masek, J.; Kovalskyy, V. Continental-scale validation of modis-based and ledaps landsat etm+ atmospheric correction methods. *Remote Sensing of Environment* **2012**, *122*, 175-184.
18. Gao, B.-C.; Montes, M.J.; Davis, C.O.; Goetz, A.F. Atmospheric correction algorithms for hyperspectral remote sensing data of land and ocean. *Remote Sensing of Environment* **2009**, *113*, S17-S24.
19. Janzen, D.T.; Fredeen, A.L.; Wheate, R.D. Radiometric correction techniques and accuracy assessment for landsat tm data in remote forested regions. *Canadian Journal of Remote Sensing* **2006**, *32*, 330-340.
20. Watmough, G.R.; Atkinson, P.M.; Hutton, C.W. A combined spectral and object-based approach to transparent cloud removal in an operational setting for landsat etm+. *International Journal of Applied Earth Observation and Geoinformation* **2011**, *13*, 220-227.
21. Wu, J.; Wang, D.; Bauer, M.E. Image-based atmospheric correction of quickbird imagery of minnesota cropland. *Remote Sensing of Environment* **2005**, *99*, 315-325.
22. Vaudour, E.; Moeys, J.; Gilliot, J.; Coquet, Y. Spatial retrieval of soil reflectance from spot multispectral data using the empirical line method. *International Journal of Remote Sensing* **2008**, *29*, 5571-5584.
23. Xu, J.-F.; Huang, J.-F. Empirical line method using spectrally stable targets to calibrate ikonos imagery. *Pedosphere* **2008**, *18*, 124-130.
24. Hadjimitsis, D.G.; Papadavid, G.; Agapiou, A.; Themistocleous, K.; Hadjimitsis, M.; Retalis, A.; Michaelides, S.; Chrysoulakis, N.; Toulios, L.; Clayton, C. Atmospheric correction for satellite remotely sensed data intended for agricultural applications: Impact on vegetation indices. *Natural Hazards and Earth System Science* **2010**, *10*, 89-95.

25. Manakos, I.; Liebler, J.; Schneider, T. Parcel based calibration of remote sensing data for precision farming purposes. *Proceedings: Angewandte Geographische Informationsverarbeitung XII* **2000**, 333-344.
26. Hadjimitsis, D.G.; Clayton, C.; Retalis, A. The use of selected pseudo-invariant targets for the application of atmospheric correction in multi-temporal studies using satellite remotely sensed imagery. *International Journal of Applied Earth Observation and Geoinformation* **2009**, *11*, 192-200.
27. Kotchenova, S.Y.; Vermote, E.F.; Matarrese, R.; Klemm Jr, F.J. Validation of a vector version of the 6s radiative transfer code for atmospheric correction of satellite data. Part i: Path radiance. *Applied optics* **2006**, *45*, 6762-6774.
28. Berk, A.; Anderson, G.P.; Bernstein, L.S.; Acharya, P.K.; Dothe, H.; Matthew, M.W.; Adler-Golden, S.M.; Chetwynd Jr, J.H.; Richtsmeier, S.C.; Pukall, B. In *Modtran4 radiative transfer modeling for atmospheric correction*, SPIE's International Symposium on Optical Science, Engineering, and Instrumentation, 1999; International Society for Optics and Photonics: pp 348-353.
29. Richter, R. In *Atmospheric correction of dais hyperspectral image data*, Aerospace/Defense Sensing and Controls, 1996; International Society for Optics and Photonics: pp 390-399.
30. Richter, R. Correction of satellite imagery over mountainous terrain. *Applied Optics* **1998**, *37*, 4004-4015.
31. Richter, R.; Schläpfer, D. Geo-atmospheric processing of airborne imaging spectrometry data. Part 2: Atmospheric/topographic correction. *International Journal of Remote Sensing* **2002**, *23*, 2631-2649.
32. Richter, R.; Schläpfer, D. Atmospheric/topographic correction for satellite imagery. *DLR report DLR-IB* **2005**, 565-501.
33. Adler-Golden, S.M.; Matthew, M.W.; Bernstein, L.S.; Levine, R.Y.; Berk, A.; Richtsmeier, S.C.; Acharya, P.K.; Anderson, G.P.; Felde, J.W.; Gardner, J.*, et al.* In *Atmospheric correction for shortwave spectral imagery based on modtran4*, SPIE's International Symposium on Optical Science, Engineering, and Instrumentation, 1999; pp 61-69.
34. Adler-Golden, S.; Berk, A.; Bernstein, L.; Richtsmeier, S.; Acharya, P.; Matthew, M.; Anderson, G.; Allred, C.; Jeong, L.; Chetwynd, J. In *Flaash, a modtran4 atmospheric correction package for hyperspectral data retrievals and simulations*, Proc. 7th Ann. JPL Airborne Earth Science Workshop, 1998; pp 97-21.
35. Manakos, I.; Manevski, K.; Kalaitzidis, C.; Edler, D. In *Comparison between atmospheric correction modules on the basis of worldview-2 imagery and in situ spectroradiometric measurements*, 7th EARSeL SIG Imaging Spectroscopy workshop, Edinburgh, 2011; pp 11-13.
36. Kampe, T.U.; Johnson, B.R.; Kuester, M.; Keller, M. Neon: The first continental-scale ecological observatory with airborne remote sensing of vegetation canopy biochemistry and structure. *Journal of Applied Remote Sensing* **2010**, *4*, 043510-043510.
37. Krause, K.; Kuester, M. Airborne observation platform (aop) pathfinder 2010 data release. http://neoninc.org/pds/files/NEON.AOP.015068.pdf.
38. Kampea, T.; Krausea, K.; Meiera, C.; Barnetta, D.; McCorkela, J. The neon 2010 airborne pathfinder campaign in florida. 2010.
39. Richter, J.; Schläpfer, D. In *Atmospheric / topographic correction for satellite imagery*, ATCOR-2/3 User Guide, Version 8.3.1, February 2014, 2014.
40. Howat, I. Envi file reader, updated 2/9/2010. http://www.mathworks.com/matlabcentral/fileexchange/15629-envi-file-reader--updated-2-9-2010.
41. Tucker, C.J. Red and photographic infrared linear combinations for monitoring vegetation. *Remote sensing of Environment* **1979**, *8*, 127-150.

42. Jackson, R.; Slater, P.; Pinter Jr, P. Discrimination of growth and water stress in wheat by various vegetation indices through clear and turbid atmospheres. *Remote sensing of environment* **1983**, *13*, 187-208.
43. Cho, M.A.; Mathieu, R.; Asner, G.P.; Naidoo, L.; van Aardt, J.; Ramoelo, A.; Debba, P.; Wessels, K.; Main, R.; Smit, I.P.*, et al.* Mapping tree species composition in south african savannas using an integrated airborne spectral and lidar system. *Remote Sensing of Environment* **2012**, *125*, 214-226.